Remote Sensing of Environment 232 (2019) 111326

Contents lists available at ScienceDirect

Remote Sensing of Environment

journal homepage: www.elsevier.com/locate/rse

Tropospheric corrections for InSAR: Statistical assessments and applications to the Central United States and Mexico

Kyle D. Murray[a,*], David P.S. Bekaert[b], Rowena B. Lohman[a]

[a] Department of Earth and Atmospheric Sciences, Cornell University, Ithaca, NY, USA
[b] Jet Propulsion Laboratory, California Institute of Technology, Pasadena, CA, USA

ARTICLE INFO

Edited by Menghua Wang

Keywords:
InSAR
Atmosphere
Tropospheric noise
Corrections
weather models
GACOS
GPS
MODIS
elevation dependence

ABSTRACT

The rapid expansion of SAR data availability and advancements in InSAR processing methods has enabled the formation of ground displacement time series for many parts of the world where such research was previously hindered by decorrelation due to sparse temporal sampling and SAR operating frequency. In particular, free and open data access from the European Sentinel-1 constellation and the future NASA-ISRO SAR (NISAR) mission is encouraging the global community to move towards automated, cloud-based processing that can accommodate these rapidly growing data volumes and facilitate the use of a suite of corrections to the data. A key challenge is related to path delays introduced when the radar signal propagates through the troposphere. Tropospheric corrections estimated from empirical, phase-based methods and those using independent data from weather models, GPS, and radiometers have been included in open-source packages such as TRAIN, PyAPS and GACOS. Users within the InSAR community have reported varying degrees of success using these methods in a range of areas around the world. However, the various statistical metrics used to evaluate the reliability of tropospheric corrections are not consistently applied and often depend on the area and the spatial scale over which they are evaluated. Examination of a simple metric such as the overall reduction in phase variability within an interferogram does not allow the user to determine whether the improvement was at large or short length scales. We present a review of existing tropospheric correction methods and statistical performance metrics, providing guidelines for global assessment and verification of the efficacy of tropospheric correction methods. We summarize the assumptions and limitations for each correction method as well as each statistical performance metric. We examine two regions with different atmospheric characteristics - one Sentinel-1 swath covering the central United States and one swath covering south central Mexico, including part of the Pacific coast. As the SAR community moves towards reliance on global and automated InSAR processing platforms that incorporate tropospheric corrections, approaches such as those examined here can aid researchers in their efforts to evaluate such corrections and include their uncertainties in derived products such as surface displacement time series, coseismic offsets, processes that correlate with topography, and signals with smaller magnitude or larger spatial scales such as those associated with small earthquakes, aseismic creep and slow slip events. We found that the GACOS products (leveraging the operational high resolution ECMWF weather model) outperform the other correction methods explored here on average, but this result is highly dependent on location, acquisition time, and data availability. We found spatial structure functions to be most useful for performance assessment because of their ability to convey information about performance at discrete spatial scales.

1. Introduction

Interferometric Synthetic Aperture Radar (InSAR) places constraints on deformation of the earth's crust in response to a wide range of processes. InSAR is often applied to problems with a large signal to noise ratio such as large, shallow earthquakes (e.g., Massonnet et al., 1993; Pritchard et al., 2002; Talebian et al., 2004; Funning et al., 2005; Lindsey et al., 2015), extraction of subsurface fluids (e.g., Amelung et al., 1999; Jones et al., 2016; Chaussard et al., 2017; Bekaert et al., 2017; Murray and Lohman, 2018), volcanic unrest (e.g., Wicks et al., 1998; Pritchard and Simons, 2002; Wicks et al., 2002; Lundgren et al., 2004; Lu and Dzurisin, 2010) or for processes with smaller magnitude but for which longer time-series exist and where averaging can reduce the impact of atmospheric noise (e.g., Goldstein, 1995; Zebker et al.,

* Corresponding author.
E-mail addresses: kdm95@cornell.edu (K.D. Murray), David.Bekaert@jpl.nasa.gov (D.P.S. Bekaert), rbl62@cornell.edu (R.B. Lohman).

https://doi.org/10.1016/j.rse.2019.111326
Received 5 March 2019; Received in revised form 1 July 2019; Accepted 15 July 2019
Available online 26 July 2019

1997; Fialko, 2006; Lindsey et al., 2014; Hussain et al., 2018). However, there are an increasing number of displacement signals of interest to the scientific community that are near or below the detection threshold, even with more modern, frequent SAR acquisitions. Recent advancements in InSAR processing methods such as persistent/permanent scatterers (PS), small baselines (SBAS), squeesar, etc., as well as an increase in the availability of temporally dense time series, has enabled the formation, and improved the quality, of ground displacement time series for an expanding range of regions across the earth (Ferretti et al., 2001; Hooper et al., 2004; Lanari et al., 2007; Ferretti et al., 2011; Hetland et al., 2012; Agram et al., 2013). However, in many cases, InSAR studies are still severely limited by spatially correlated noise resulting from radar path delays as signals are refracted and scattered through the troposphere. Properly characterizing this noise remains a challenge and reduces the ability of researchers to take full advantage of the available InSAR time series (e.g., Hooper et al., 2012).

Tropospheric corrections using empirical phase-based methods (e.g., Beauducel et al., 2000; Lin et al., 2010; Bekaert et al., 2015a), independent data from weather models, GPS, and radiometers are available in open-source packages and datasets such as TRAIN, PyAPS and the Generic Atmospheric Correction Online Service for InSAR (GACOS) (Jolivet et al., 2011; Bekaert et al., 2015c; Yu et al., 2018), and have been implemented with variable degrees of success (Li et al., 2005; Foster et al., 2006; Elliott et al., 2008; Bekaert et al., 2015b; Fielding et al., 2017). In many cases these corrections are applied without evaluation of their performance or the impact of the correction. Validation of these corrections has not been emphasized, and in many cases, is ignored or performed using simple metrics such as the reduction in overall variance of individual interferograms. Efforts to study signals with low signal-to-noise ratios globally require the development and assessment of methods for modeling the contribution to SAR interferograms from the troposphere as well as routine methods for assessing their performance. Here we present a review of techniques (Table 1) used to model and reduce the impact of tropospheric delays on InSAR observations with a comparison of common statistical methods used to assess their quality.

1.1. Study regions

We explore corrections in two areas that sample very different tropospheric conditions, and where the atmospheric corrections may be expected to perform very differently: the central US and south-central Mexico.

The central US is located thousands of kilometers from the nearest plate-boundary, but the frequency and magnitude of seismic events in much of this region have dramatically increased in the last decade (e.g., Keranen and Weingarten, 2018). This increase has been tied to anthropogenic activity, including wastewater injection (e.g., Holland, 2013; Horton, 2012), which has increased since the early 2000's (e.g., Ellsworth, 2013). Few studies have been performed using InSAR in the central US or similar areas, however, in part because of strong phase delays associated with the troposphere which are often an order of magnitude larger (10's of cm) than the signal expected from the largest earthquakes in this region (< 3 cm) (Fielding et al., 2017; Grandin et al., 2017; Yeck et al., 2017; Barnhart et al., 2018).

The central US is a region with limited topographic relief that experiences very strong gradients in tropospheric properties and where there are numerous observations available for assimilation into weather reanalysis products (e.g., Dee et al., 2011). Large weather fronts are particularly common in such mid-latitudinal regions where air masses from the north and south meet (e.g., Carlson, 1991), often associated with destructive hail, heavy rain or tornadoes. These types of storms cause decorrelation and phase delays in interferograms, both from disturbance to the ground surface and through large gradients in the refractive delays within the troposphere. We explore this area with 61C-band SAR images acquired between March 13, 2015 and February 25,

Table 1
Examples of correction datasets and their characteristics.

Dataset	Description	Data product	Spatial resolution	Coverage	Temporal sampling	Hydrostatic delay	Wet delay
GPS	Propagation delay	Zenith total delay	Station spacing	Global	5 min	Yes	Yes
InSAR (Sentinel-1)	Propagation delay	Phase change (empirical)	5–20 m	Global	6–24 days	Yes	Yes
AQUA/TERRA (MODIS)	Spectroradiometer	Water vapor	1 km	Global	3 h	No	Yes
ENVISAT (MERIS)	Spectrometer	Water vapor	1.2 km	Global	35 days	No	Yes
Sentinel-3 (OLCI)	Radiometer	Water vapor	300 m	Global	1–2 days	No	Yes
MERRA	Weather reanalysis model	Pressure, temperature, humidity	50 km	Global	6 h	Yes	Yes
NARR	Weather reanalysis model	Pressure, temperature, humidity	32 km	US only	3 h	Yes	Yes
WRF model outputs	Mesoscale Numerical weather model	Pressure, temperature, humidity	Variable	Global	Variable	Yes	Yes
ERA-I	Weather reanalysis model	Pressure, temperature, humidity	75 km	Global	6 h	Yes	Yes
GACOS	Operational weather model	Pressure, temperature, humidity	14 km	Global	6 h	Yes	Yes
NEXRAD	Weather Radar	Precipitation Reflectivity	10 s–100 s km	US only	5 min	No	No

Fig. 1. Overview of the study area covering both the central US and south central Mexico. We use 61 and 41 acquisitions from the central US and Mexico, respectively from Sentinel-1 satellite (red boxes) acquired between March 2015 and February 2018. Dashed vector shows satellite flight direction with orthogonal line-of-site (LOS) vector for both areas. (For interpretation of the references to color in this figure legend, the reader is referred to the web version of this article.)

2018, by the Sentinel-1a/b satellites (path 144; Fig. 1), part of ESA's Copernicus Program (De Zan and Guarnieri, 2006; European Space Agency, 2013), covering an area of approximately 250 km by 550 km.

Our other study region in south-central Mexico includes a plate boundary zone with active subduction and volcanism. Crustal deformation is expected from the seismic cycle (e.g., Bekaert et al., 2015b), volcanic processes (e.g., Chaussard et al., 2013), as well as anthropogenic activity such as groundwater pumping (e.g., Osmanoğlu et al., 2011). Our study area covers an area of approximately 250 km by 550 km, stretching from the southern Pacific coast at sea level to mountainous regions exceeding 4 km elevation. This area experiences large gradients in tropospheric properties between the coast and inland areas related to elevation-correlated phase delays. The coastal mountain range (Sierra Madre del Sur) reaches approximately 2 km and acts as a barrier to coastal winds, resulting in unique tropospheric properties on either side of the range (e.g., Bekaert et al., 2015a). We explore this area with 41C-band SAR images from the Sentinel-1a/b satellites (path 078; Fig. 1) from March 28, 2015 to February 4, 2018.

We processed all SAR imagery using the InSAR Scientific Computing Environment (ISCE) (Rosen et al., 2012) stack processing capability (Fattahi et al., 2017). We down-looked the interferograms to a spatial resolution of 300 m for both Central US and Mexico. SAR images used in our study were acquired at 00:28 UTC time (Central US) and 00:48 UTC time (Mexico).

1.2. Components of tropospheric SAR delays

The tropospheric delay is a result of refraction of the radar signal during propagation through the troposphere, and is often separated into a hydrostatic and a wet component (e.g., Berrada Baby et al., 1988; Bevis et al., 1992). The hydrostatic component depends on pressure and temperature and tends to vary smoothly in space over long length scales (> 100 km) and generally varies slowly with time (e.g., Hanssen and Bamler, 1999). The wet component depends on variations in water vapor and temperature. The impact on InSAR from these components can be much smaller than the impact on individual SAR images because characteristics of the delay that are stationary in time (e.g., the variation with elevation) cancel out leaving only the difference between the two dates. In general, pressure and temperature vary much less in time and space than does water vapor content. Therefore, while the magnitude of the hydrostatic delay on a particular date is larger than the magnitude of the wet component, the impact of the wet component on interferograms is larger than the hydrostatic component.

The refractivity of the two-way radar path through a given layer of the troposphere is calculated using the total atmospheric pressure (P) (hPa^{-1}), the partial pressure of water vapor (e) (hPa^{-1}), and temperature (T) (K) as:

$$N = \left(k_1 \frac{P}{T}\right)_{hydr} + \left(k_2 \frac{e}{T} + k_3 \frac{e}{T^2}\right)_{wet} = N_{hydr} + N_{wet} \quad (1)$$

The coefficients k_1, k_2 and k_3 are empirical constants which we take as $k_1 = 77.6\ K\ hPa^{-1}$, $k_2 = 23.3\ K\ hPa^{-1}$ and $k_3 = 3.75 \cdot 105\ K^2\ hPa^{-1}$ (Smith and Weintraub, 1953). N is then converted to a total SAR delay (ϕ_{tropo}) (meters) by integrating through all layers (h) of the atmosphere from the bottom (h_1) to the top (h_{top}) along the radar line-of-sight as:

$$\phi_{trop} = \frac{-4\pi}{\lambda} \frac{10^{-6}}{cos\theta} \int_{h1}^{h_{top}} (N_{hydr} + N_{wet}) dh \quad (2)$$

where θ is the satellite incidence angle and λ is the radar wavelength (e.g., Hanssen, 2001).

The spatio-temporal characteristics of tropospheric delays change significantly depending on the region of the world being studied, making automated, routine corrections to interferograms quite challenging. Below, we summarize the wide range of correction techniques used to address these different components (Table 1).

2. Tropospheric correction methods

Correction methods are typically split into those estimated from the data themselves, i.e., phase-based methods, and those using independent constraints on atmospheric properties. Below we provide an overview of the different methods. For each, we include a brief summary of their advantages and disadvantages at the end of each section.

An interferogram between two SAR acquisitions at times t_1 and t_2, is impacted by contributions from the troposphere, displacement of the ground surface, and other sources of noise:

$$\Delta\phi_{tot} = (\phi_{trop}^{t_2} - \phi_{trop}^{t_1}) + \Delta\phi_{def}^{t_{12}} + \Delta\phi_{other}^{t_{12}} \quad (3)$$

where $\Delta\phi_{def}^{t_{12}}$ is the unwrapped phase related to deformation during the time period between t_1 and t_2, and $\Delta\phi_{other}^{t_{12}}$is the unwrapped phase related to other unmodeled sources contributing to phase changes such as ionospheric effects, soil moisture, unwrapping errors, etc. The corrected interferometric phase delay can be computed by combining LOS profiles of temperature, pressure, and water vapor partial pressure (Eq. (2)) from two acquisitions at times t_1 and t_2, and subtracting it from the original unwrapped interferogram as:

$$\Delta\phi^* = \Delta\phi_{tot} - (\phi_{trop}^{t_2} - \phi_{trop}^{t_1}) \quad (4)$$

We show the resulting corrected interferograms, $\Delta\phi^*$, and compare several metrics for assessing the degree to which the signal has been reduced in section 4.

2.1. Corrections using weather model products

Weather model outputs include pressure, temperature and specific humidity, which can be used to compute the total (hydrostatic and wet) tropospheric delays in the radar line-of-sight (e.g., Doin et al., 2009; Jolivet et al., 2011; Bekaert et al., 2015c). Various off-the-shelf models

can be used as input for tropospheric corrections, including weather reanalysis products and operational forecasting models. The spatial-temporal sampling is model specific, and ranges from global to regional analysis, and temporal sampling from 6 h to hourly. Locally run forecast products using mesoscale models (e.g., the Weather Research and Forecasting, or WRF model) can also be applied to InSAR data (e.g., Bekaert et al., 2015c) by users with the capability to implement them. These types of models are used for forecasting by default, but in our case, are also useful hindcasting tools. Although model outputs are at much coarser resolution than the InSAR data (Table 1), the estimated correction will contain structures/features at the spatial scale of the digital elevation model, due to the vertical integration of atmospheric properties from the surface upwards. In areas with high relief, the impact of variations in surface elevation may dominate the tropospheric contribution to the interferogram, while in flatter regions, the terrain-induced effects will not be as large, and the turbulent component, as well as other lateral variations in tropospheric properties (which are only sampled at the coarser resolution of the weather model), may dominate. Our two study areas are characterized by very different amounts of topographic relief, with the central US site spanning a far smaller elevation range than the site in Mexico (Figs. 3 and 4).

We test the Modern-Era Retrospective analysis for Research Applications (MERRA-2), European Reanalysis-Interim (ERA-I), North American Regional Reanalysis (NARR), and GACOS (Yu et al., 2018) ECMWF-operation models. A summary of the spatial temporal characteristics of each model is contained in Table 1. We use each model to estimate the tropospheric contribution on each available SAR date, with examples for the two study areas for one interferometric pair each shown in Figs. 5 and 6. Note that the timescale associated with each product differs (Table 1, Fig. 2). We apply a linear interpolation in time between the two outputs spanning the SAR acquisition time to better account for temporal tropospheric variations.

Advantages

- Independent estimate of tropospheric properties
- Global weather model outputs and reanalysis products readily available
- Available off-the-shelf

Disadvantages

- Coarse spatial-temporal sampling of global models, localized model require in-depth experience to set-up and run
- Temporal sampling may result in several hour time differences between model outputs and SAR acquisition
- Models may perform poorly in the presence of cloud cover
- Often not immediately available
- Spatial scale is coarse w.r.t the wet component typically observed in SAR interferograms

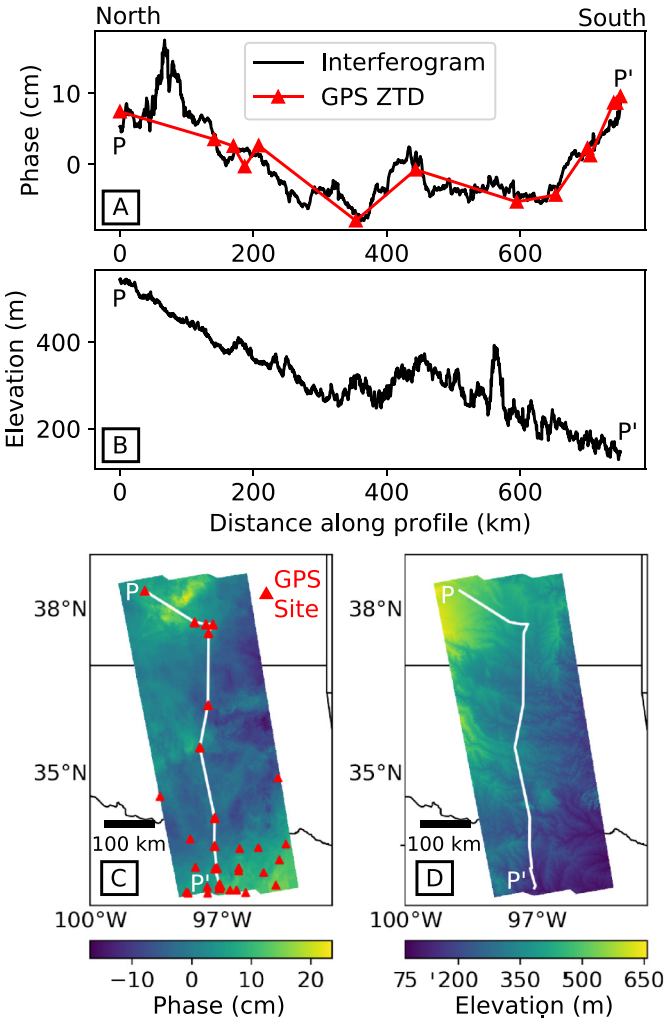

Fig. 3. Elevation dependence in central US (A) Phase variation along white profile line (C) connecting a string of GPS sites (red triangles). (B) Elevation variation along profile shown in D. (C) Interferogram (color, 07/17/2016–07/29/2016) and available GPS sites (red triangles). (D) Elevation (color) from SRTM-DEM (Farr et al., 2007). (For interpretation of the references to color in this figure legend, the reader is referred to the web version of this article.)

2.2. Correction using precipitable water vapor retrieval products

Precipitable water vapor (PWV) is defined as the column height of liquid water equivalent to the total water vapor present between Earth's surface and the top of the atmosphere (Bevis et al., 1992):

$$PWV = \frac{1}{\rho_w R_v} \int_h^\infty \frac{e}{T} dh, \tag{5}$$

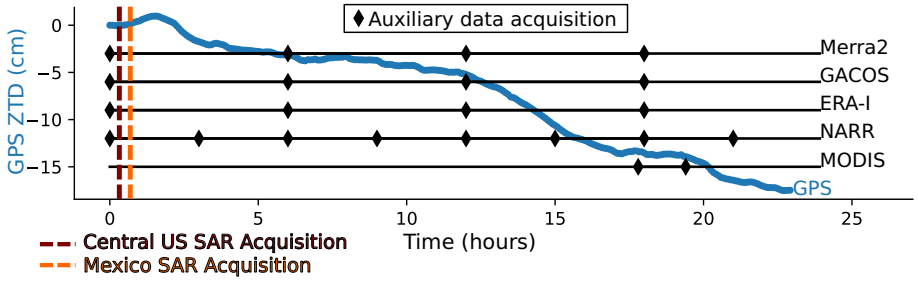

Fig. 2. 24 h GPS time series (blue) on 07/17/2016 in central US and timeline of independent data acquisitions (diamonds). SAR acquisitions times are shown in red and orange vertical dashed lines. (For interpretation of the references to color in this figure legend, the reader is referred to the web version of this article.)

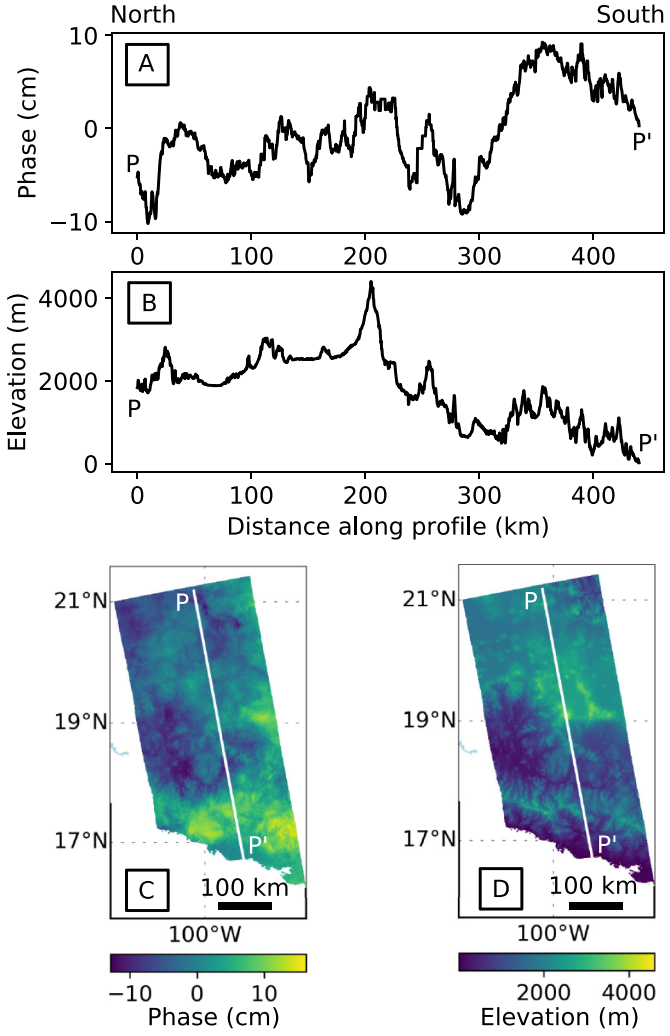

Fig. 4. Elevation dependence in Mexico. (A) Phase variation along white profile line from (C). (B) Elevation variation along white profile line from (D). (C) Interferogram (color, 4/15/2016–5/9/2016). (D) Elevation (color) from SRTM-DEM (Farr et al., 2007). (For interpretation of the references to color in this figure legend, the reader is referred to the web version of this article.)

where ρ_w is the density of water, e is the elevation of the Earth's surface, R_v is the specific gas constant for water vapor, and T is temperature. PWV can be related to the wet component of SAR phase delay, Φ_{tropo}^{wet}, by:

$$\phi_{tropo}^{wet} = \frac{-4\pi}{\lambda}\frac{\Pi}{cos(\theta)}PWV, \quad (6)$$

where λ is the radar wavelength, θ is the incidence angle of the SAR satellite and the empirical conversion factor Π is typically ~6.2 but varies with tropospheric temperature (e.g., Bevis et al., 1992; Li et al., 2003, 2005).

PWV products are available from NASA's MODIS (Moderate Resolution Imaging Spectroradiometer), and the European Space Agency's (ESA) MERIS (MEdium Resolution Imaging Spectrometer) and Copernicus Constellation Sentinel-3 A and B OLCI (Ocean and Land Colour Instrument). PWV methods based on spectrometers are computed using radiance ratios between frequency bands that have different sensitivities to water vapor. For both of our study areas, we include an example of a tropospheric correction using MODIS data, whenever images were acquired within eight hours of the SAR image acquisition (Figs. 5 and 6).

Advantages

- Independent estimate of tropospheric properties
- Observation of the atmospheric state, not a model

Disadvantages

- Temporal sampling often quite different than SAR image acquisition times
- No retrieval (or degraded quality) at night or in areas with cloud cover
- Inaccurate cloud masking can result in strong biases

2.3. Corrections estimated from GNSS

Estimates of the Zenith Total Delay (ZTD) are a product of Global Positioning System (GPS) and Global Navigation Satellite System (GNSS) processing, and can be used to validate other independent datasets at points, or can be spatially interpolated to directly correct SAR imagery when the GNSS network is spatially dense and well distributed (e.g., Bevis et al., 1992; Li et al., 2005; Onn and Zebker, 2006; Reuveni et al., 2015; Houlié et al., 2016). Continuous GPS provides high temporal resolution (Fig. 2) and is, therefore, effective at predicting delays in areas where weather patterns vary rapidly over timescales that would otherwise be aliased in the case of other independent datasets considered here (e.g., Yu et al., 2018). Corrections using GPS are limited by the density and distribution of the GPS network, usually providing little constraint on shorter-spatial-scale, turbulent signals. Furthermore, it is often desirable to separate the wet component from the hydrostatic component in the ZTD, which requires additional independent data or assumptions about how much each individual component contributes to the ZTD.

We show results using ZTD estimates for the central US site that are freely available from the Nevada Geodetic Laboratory at the University of Nevada Reno (http://geodesy.unr.edu) (Blewitt et al., 2018). We do not include GPS/GNSS results for the Mexico site, due to the lack of a dense network of continuous sites.

Advantages

- Independent estimate of tropospheric properties
- Continuous, dense temporal sampling

Disadvantages

- Non-global coverage
- Only samples troposphere in the vicinity of individual GPS sites

2.4. Corrections estimated from the InSAR phase

The goal of empirical, phase-based methods is to separate signals of geophysical interest from the tropospheric phase component. The InSAR community often splits the tropospheric noise into the following components based on their spatial scale and correlation with elevation: (1) the topography correlated delay, (2) the long spatial-scale components of the delay, and (3) the turbulent component of the delay, which results from small-scale, irregular air motions that vary over 3-dimensional distances smaller than a few 10's of km (e.g., Emardson et al., 2003). In regions with high relief, phase delays are often strongly correlated with elevation. Various approaches have been developed and applied including estimation of a linear or power-law correction in a non-deforming area (e.g., Remy et al., 2003; Cavalie et al., 2007; Elliott et al., 2008), or multiscale approaches in which the correlation is estimated from a spatial band not dominated by the deformation signal (e.g., Bekaert et al., 2015a; Lin et al., 2010).

Phase-based corrections using a network-based approach that capitalizes on the dense InSAR time series now available also show great promise for reducing the impact of tropospheric noise on InSAR time series (e.g., Tymofyeyeva and Fialko, 2015; Liang et al., 2018). Here,

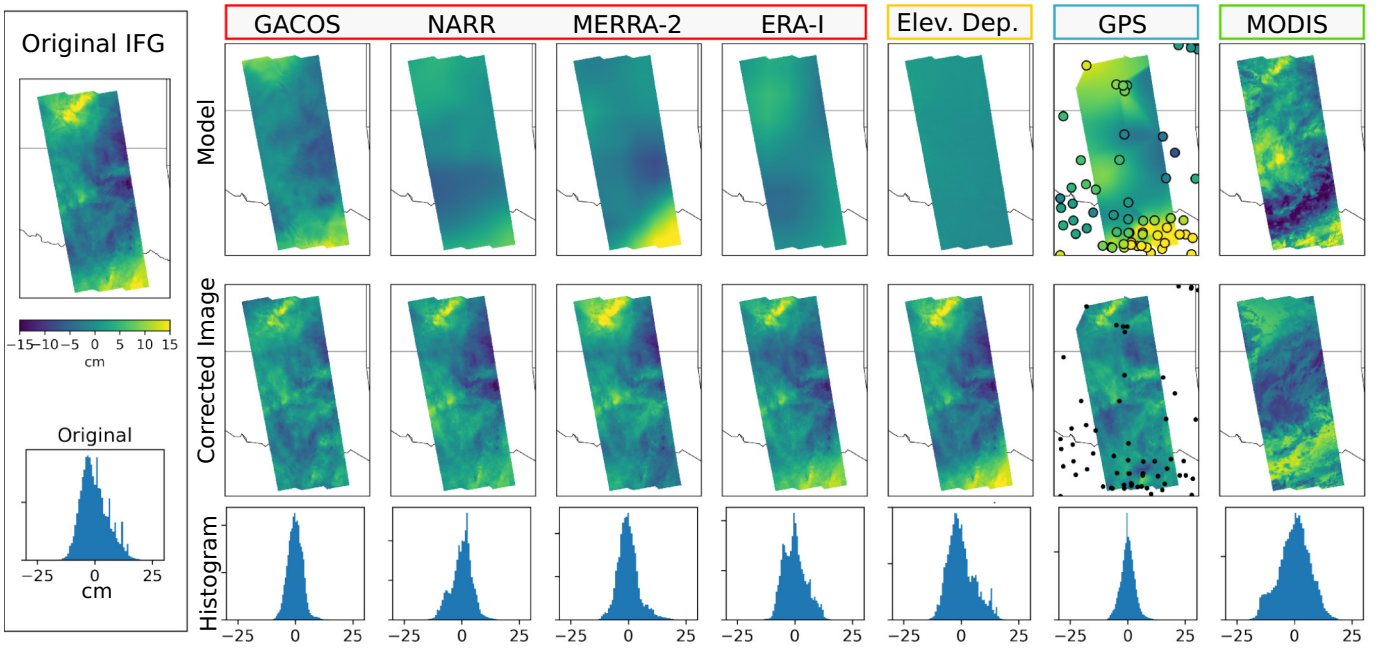

Fig. 5. Central US Example: Interferogram (upper left) for date pair 07/17/2016–07/29/2016, modeled tropospheric delays using various independent datasets (1st row), corrected interferogram for each correction type (2nd row), and histograms for each corrected interferogram (3rd row). Column headings are grouped by weather models (red), phase-elevation dependence (yellow), GNSS (blue), and precipitable water vapor data (green). (For interpretation of the references to color in this figure legend, the reader is referred to the web version of this article.)

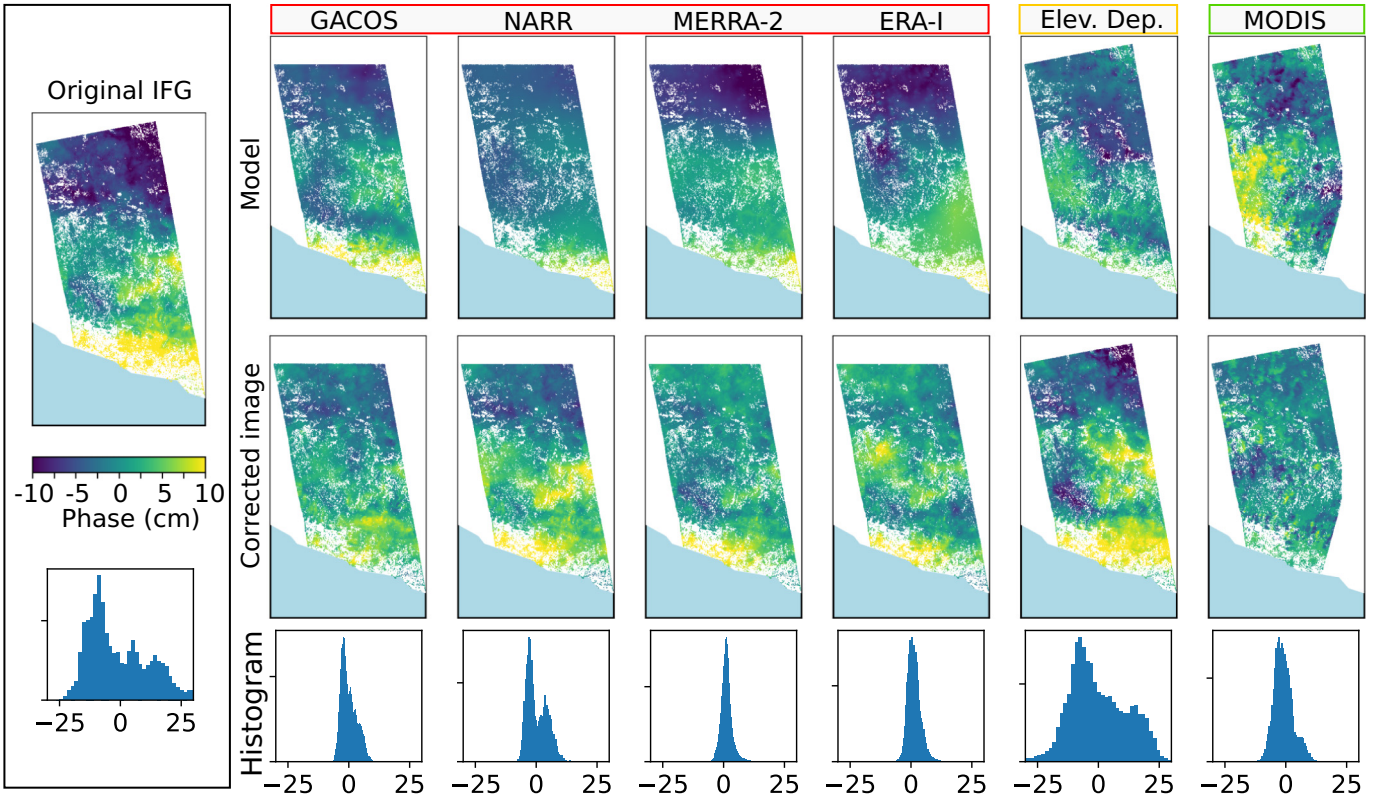

Fig. 6. Mexico example: Interferogram (left) for date pair 3/5/2017–3/17/17, modeled tropospheric delays using various independent datasets for that interferogram (1st row), and corrected interferogram for each correction type (2nd row). Column headings are grouped by weather models (red), phase-elevation dependence (yellow), and precipitable water vapor data (green). (For interpretation of the references to color in this figure legend, the reader is referred to the web version of this article.)

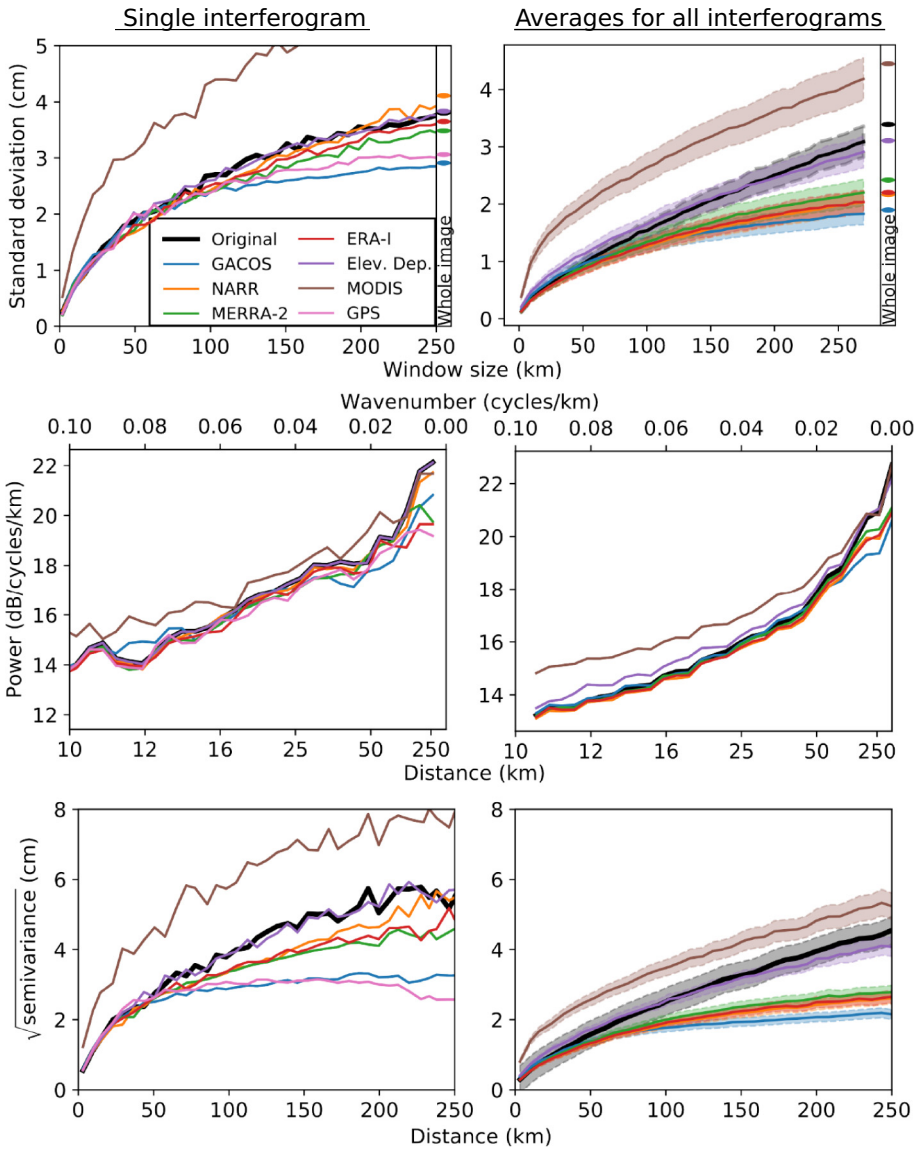

Fig. 7. Central US results: Statistical metrics as a function of distance for example interferogram (07/17/2016–07/29/2016) before and after applying corrections (left column) and the same metrics averaged over 60 interferograms made from 61 dates (right column). Average standard deviation as a function of the size of a square window of pixels (row 1), spectral characteristics (row 2), and semivariograms (row 3) for each correction type. GPS results were excluded from averaged metrics (right column) due to variability in data availability throughout the date range.

we include the simpler phase-elevation relationship for comparison primarily to emphasize the difference in performance between areas with and without significant topography. There are many scenarios, particularly for studies that focus on smaller spatial scales, where the simpler phase-elevation relationships mitigate the impact of the troposphere to a sufficient degree. For more subtle signals, researchers can even combine phase-elevation relationships and weather model products to capitalize on the strengths of both approaches (e.g., Shen et al., 2019).

One way to address the long spatial-scale components of the delay is to remove simple polynomial functions (ramps) from interferograms (e.g., Lohman and Simons, 2005). This method can be effective at removing unwanted long wavelength signals from troposphere, ionosphere, and oribital errors. However, this method does not reduce the impact of turbulent tropospheric signals and can introduce additional noise to the interferogram, particularly when the deformation signal of interest also covers large spatial scales (e.g., Murray and Lohman, 2018). The removal of simple polynomial functions is not well suited for deformation processes where strain across large spatial scales is expected. Researchers can use a reference network such as GNSS, if available, to correct for known deformation signals with large spatial scales before the removal of polynomial functions. The corrections would then be expected to represent tropospheric/ionospheric contributions to the signal or, in the case of older SAR imagery, residuals related to the inaccuracy of satellite orbit estimates. In our analysis we have not removed any long wavelength function from the interferograms so that we can assess the performance of the mitigation approaches at the larger spatial scales that are often targeted (e.g., studies of interseismic deformation or postseismic responses for subduction zone events). Orbital errors in Sentinel-1 data are insignificant relative to the magnitude of atmospheric delays (e.g., Fattahi and Amelung, 2014). Furthermore, we inspected interferograms for ionospheric delays – which would be apparent as discontinuities at burst boundaries – and did not find severe cases.

For each of our sites, we include an example where we have removed a linear relationship between phase and elevation, using the best-fit parameters averaged across each interferogram in a least-squares sense. As expected, the impact of this empirical correction is

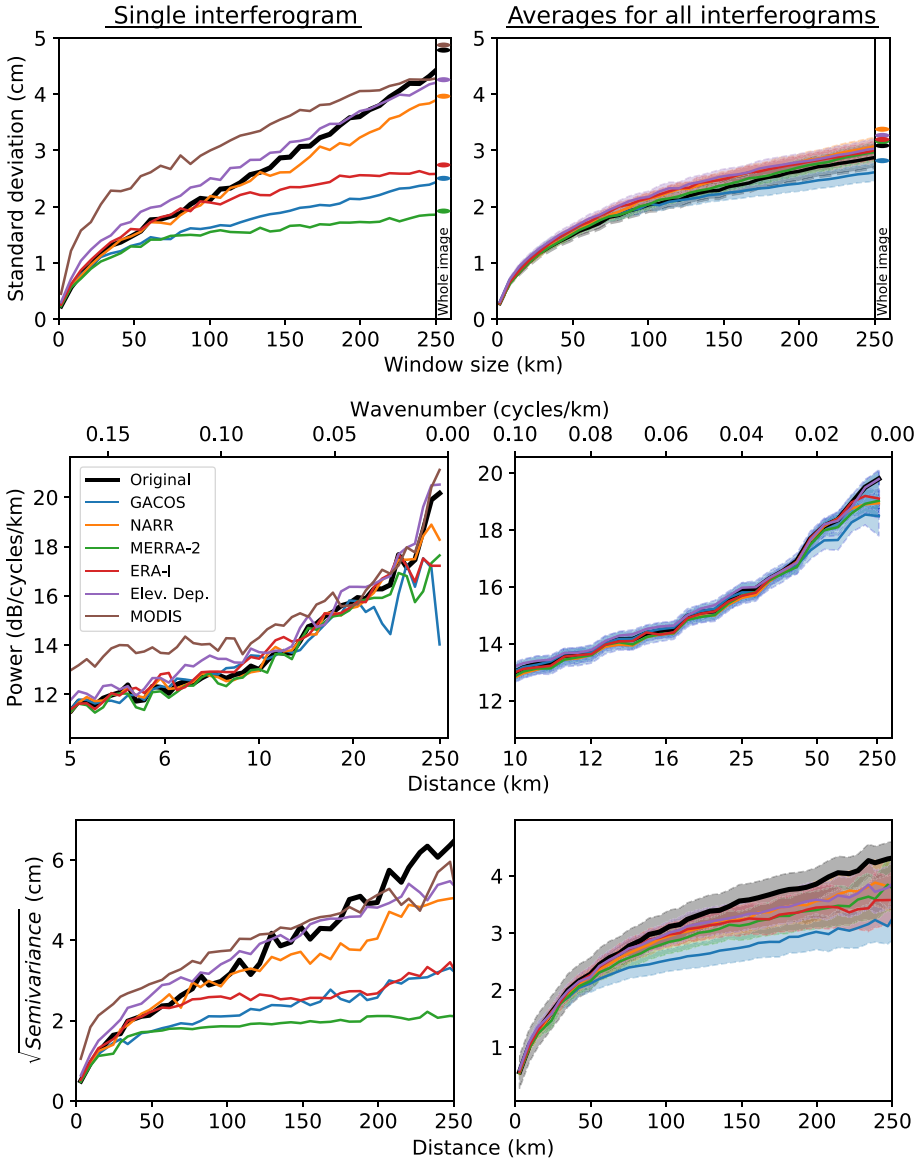

Fig. 8. Mexico results: Statistical metrics as a function of distance for example interferogram (3/5/2017–3/17/2017) before and after applying corrections (left column) and the same metrics averaged over 60 interferograms made from 61 dates (right column). Average standard deviation as a function of the size of a square window of pixels (row 1), spectral characteristics (row 2), and semivariograms (row 3) for each correction type.

larger for the study area in Mexico, due to the larger topographic relief (Figs. 5 and 6).

Advantages

- Not dependent on the existence of independent data
- Correction is relevant to the time period of the SAR acquisitions

Disadvantages

- Requires spatial averaging to reliably estimate correlation between phase and elevation, and may average across regions with different statistical properties
- Hard to separate tropospheric noise from other superimposed signals (ground displacements, soil moisture variability), may remove signals of interest
- Predominantly used to estimate topography-correlated and large spatial-scale tropospheric noise. Does not capture turbulent delay component

3. Statistical methods for assessing the quality of corrections

The accuracy of estimated tropospheric delays depends on the properties of the troposphere in the given area of interest, the spatial and temporal scale of the area, as well as the spatial/temporal resolution and accuracy of the correction dataset or model. These dependencies contribute to the difficulty in predicting how well a given correction will perform in a given area. With a main aim to improve interferograms, the application of tropospheric phase corrections to interferograms can also lead to no improvement, or even degradation of, the original data (e.g., Li et al., 2006; Onn and Zebker, 2006; Doin et al., 2009). We assess the performance of the corrections described above using a range of statistical metrics (RMS/standard deviation, spectral analysis, and semivariograms) (Figs. 7 and 8). Our goal is to not only better understand which corrections perform better, but also which statistical metrics are the most useful and how their utility varies between study regions.

Statistical methods for assessing the quality of a tropospheric correction generally rely on some measure of the magnitude of the data

residual after application of a correction. This measure can be calculated across the entire interferogram or within regions that are expected to be non-deforming. In most cases, the statistics of the residual are assumed to be spatially stationary and isotropic, but some anisotropy can be included (e.g., Lohman et al., 2002), and most can be extended to allow for spatial variability in the case of larger study areas where the tropospheric properties are expected to vary significantly (e.g., Bekaert et al., 2015a; Scott and Lohman, 2016). The measures of size (described below) vary primarily in terms of whether they explicitly account for the spatial scale being considered. We summarize three types of commonly-used metrics, and then show examples of the metrics applied to a single interferogram (Figs. 6 and 7, left column) and then to all of the interferograms for each of our two study areas (Figs. 6 and 7, right column).

The simplest, and most commonly used metric, is the root-mean-square (RMS) or standard deviation of the residual signal (e.g., Remy et al., 2003; Puysségur et al., 2007; Doin et al., 2009). We note that this is also the metric that is implicitly chosen in most empirical fits, i.e., best-fit phase vs. elevation relationships. The RMS of the corrected interferogram $\Delta\phi^{*}$ estimated over a sample window containing n pixels is:

$$\Delta\phi^{*}_{RMS} = \sqrt{\frac{1}{n}\sum^{n}\Delta\phi^{*2}} \tag{7}$$

If the mean value of the sample is removed, the RMS is simply the standard deviation (σ) of the sample. In our test we examine the standard deviation of the interferograms, before and after applying a correction, over a range of spatial scales. For each window size we take the average of the standard deviation of 200 windows randomly sampling the interferogram. The range of the 200 translations for a given window size is increasingly limited as the window size approaches the image dimensions. Thus, more redundant pixels are sampled by larger windows. For these tests (Figs. 7 and 8, top row), we include the standard deviation of the entire region for reference (Figs. 7 and 8, far right).

The RMS/standard deviation of a given window does not contain any information about the spatial structure of the signal within that window. For example, white, normally distributed noise could have the same RMS/standard deviation as a linear ramp. Another approach that attempts to separate out the spatial scales that contribute to the noise is frequency domain analysis (e.g., Goldstein, 1995; Hanssen, 2001; Foster et al., 2006; Li et al., 2007). Frequency domain analysis usually requires filling of any data gaps within the interferogram so that standard fast Fourier transform (FFT) approaches can be used. Similarly to how the RMS approach is limited as the window size approaches the image dimensions, another limitation of the FFT approach is that the output is restricted to specific wavenumbers that are defined by the size of the image, with far more samples at the shorter spatial scales than at larger spatial scales. Here, we apply an FFT after nearest-neighbor void-filling to each interferogram and compute the average power as a function of spatial scale (Figs. 7 and 8, middle row).

Finally, we examine the use of spatial structure functions, which represent the variability of the data as a function of distance between pairs of data points (e.g., Williams et al., 1998; Hanssen and Bamler, 1999; Lohman and Simons, 2005). Structure functions allow us to explicitly separate the impact of the correction on different length scales, and are not limited by the existence of gaps or irregularly-spaced data points. We focus on the type of spatial structure function that is also referred to as a semi-variogram, defined as:

$$S(\boldsymbol{r}) = E[(\Delta\phi^{*}(\boldsymbol{x}) - \Delta\phi^{*}(\boldsymbol{x}+\boldsymbol{r}))^{2}], \tag{8}$$

where $\phi(\boldsymbol{x})$ is the phase, or residual phase, at position $\boldsymbol{x}$ in the interferograms and $\boldsymbol{r}$ is a distance vector. In this paper, we only consider the impact of the length of $\boldsymbol{r}$, although the azimuthal dependence can also be examined (e.g., Lohman and Simons, 2005). Semivariograms have several useful characteristics that allow the user to evaluate spatial structure. The semivariogram often approaches a maximum value after a distance known as the range, implying there is no correlation between values separated by distances greater than the range. The value of semivariance at this distance is referred to as the sill. The square root of the value of the sill is a comparable metric to the total RMS of the image, although often larger.

We use an empirical semivariogram approach and randomly sampled pairs of data points binned by distance (Figs. 7 and 8, bottom row). In the case of data that contains signals with large spatial scales (such as from orbital errors or large-scale atmospheric effects), the semivariogram continues to increase at scales comparable to or larger than the dimensions of the interferogram, and a sill will not exist. Researchers will often remove a planar function from the image before computing the semivariogram. However, we are interested in comparing how well different correction methods account for tropospheric effects at all scales covered by our study areas. Therefore, we do not remove any functions apart from the mean value of each interferogram. Residual signals with large spatial scales may still be present due to unmodeled tropospheric, ionospheric, and/or orbital effects, or due to signals introduced by errors in the tropospheric model.

4. Results and discussion

The majority of SAR acquisitions were acquired in 12-day intervals in the central US and 24-day intervals in Mexico. All interferograms were made as sequential pairs with the shortest possible time range, ensuring the highest possible coherence, minimal unwrapping errors, and negligible amounts of crustal deformation between acquisitions. We assume unwrapping errors were negligible in the central US and data in Mexico was masked in areas of suspected unwrapping errors. We do not expect any large tectonic or anthropogenic processes within these time series, but even if such signals are present, the metrics used here should still decrease if tropospheric signals are successfully removed. Unlike historic SAR sensors, orbital errors for Sentinel-1a/b are expected to be small due to highly accurate orbit information (e.g., Fattahi and Amelung, 2014).

Interferograms in both the central US and Mexico show high temporal and spatial variability (Fig. S1). Maximum tropospheric delays range from approximately 5 to 25 cm, and standard deviations of the individual interferograms range from ~2 to ~5 cm. Approximately 17% of the interferograms in the central US contain large storm fronts covering part of our study area. These storms are characterized by spatially abrupt, large-magnitude phase changes, and active precipitation. The presence of these storms has been verified using observations from the Next-Generation Radar (NEXRAD) ground-based radar networks, which show areas of active precipitation. None of the methods in this study correct for phase delays caused by precipitation (nor potential soil moisture effects in the wake of storms), referred to in the literature as the liquid tropospheric delay (e.g., Hanssen, 2001).

4.1. Comparison of correction methods

Below, when reporting on the performance of correction methods, we comment on the reduction in overall interferogram RMS/standard deviation. Overall RMS reduction is a useful metric for rapidly assessing the general performance averaged over all spatial scales. However, we have found that the spatial semivariogram contains more useful information about specific spatial scales where any improvements may or may not occur. This information is an important complement to the RMS reduction alone, as it can be used in the evaluation of how well the dataset can constrain models of solid earth deformation that operate over a given spatial scale (e.g., Fournier et al., 2011).

Spatial semivariograms are also is an improvement over the scale-dependent standard deviation/RMS metric because the standard deviation for a window of a given size is still a function of variability at all scales smaller than the window, whereas the semivariogram contains information about discrete distance bins. For instance, in the three right panels of Fig. 7, the weather model-based corrections all result in

significant improvements starting at values greater than approximately 75 km. This can be roughly observed in the case of all three metrics, but the semivariogram shows it much more clearly because the remaining variability at scales below 75 km does not contribute to the semivariogram at larger scales in the way that it does in the scale-dependent standard deviation/RMS. The spectral analysis approach is similar to the semivariogram in that it shows information about discrete frequency ranges. This method however is less favored due to the added noise and computation of transforming between the spatial and frequency domains, the limited set of frequency ranges that are accessible from a standard FFT, and artifacts resulting from filter edges.

4.2. Elevation dependence

Due to the much larger topographic relief, interferograms in Mexico are characterized by more significant topography-correlated signal than the central US. However, on average, we find that the elevation-dependence correction has no significant effect in either study region (Figs. 7 and 8). This is likely due to either the lack of topographic relief (in the case of the central US) or the high spatial variability in how the tropospheric phase delays actually correlate with elevation. For example, the coastal mountain range in Mexico acts as a barrier to the typically more humid air coming from the Pacific ocean (e.g., Bekaert et al., 2015a). Elevation dependence has been shown to be a stronger predictor of phase in other regions of the world (e.g., Zebker et al., 1997; Elliott et al., 2008; Bekaert et al., 2015a).

4.3. Weather reanalysis model corrections

The weather model corrections resulted in variable degrees of success. On average, weather models show insignificant improvement at spatial scales shorter than approximately 75 km, despite the fact that some models have spatial resolutions of 16 km. On average, the GACOS correction using the ECMWF operational model performed the best in both study areas and lowered the average whole image standard deviation by ~2.5 cm in the central US (Fig. 7, top row) and 1.5 cm in Mexico (Fig. 8, top row). The other three models performed equivalently well when averaged over all of the available interferograms and lowered the average whole image standard deviation by ~2 cm in the central US (Fig. 7, top row) and ~1 cm in Mexico (Fig. 8, top row). All tested weather models had outputs at UTC 00:00, which are within 28 min and 48 min of the SAR acquisition times for the Central US and Mexico, respectively.

4.4. MODIS corrections

On average, MODIS-derived corrections increased the whole image standard deviation by ~1.3 cm in the central US (Fig. 7, top row) and had negligible effects in Mexico (Fig. 8, top row). MODIS-derived corrections were largely unsuccessful for a number of reasons. First, and most importantly, the available MODIS data acquisitions were not acquired close in time to the SAR acquisitions. The difference between acquisition times was often > 4 h and tropospheric properties in these regions often vary significantly over the course of hours or even minutes. Second, because MODIS is a passive spectroradiometer, we are limited by cloud cover. Clouds are often correlated in space with areas of variable and turbulent tropospheric properties, thus the spatially incomplete MODIS corrections have gaps in some of the areas with the largest tropospheric signals. Finally, MODIS data only constrains the precipitable water vapor (wet component) of the tropospheric delay. A more complete correction would require combining the MODIS imagery with independent data that constrains the hydrostatic component.

4.5. GPS

We only examined GPS corrections in the central US where the site spacing approaches the shorter spatial scales of interest in at least some parts of the study area (~10 km). The availability of GPS data for any given station in the central US was variable, thus we were not able to find the average quality of the GPS to compare to other correction methods (right column, Fig. 7). However, on a case-by-case basis, when data was available for the full network, we found that the GPS-derived corrections performed well, comparable to the GACOS model, lowering the whole image standard deviation by ~2.5 cm (Fig. 7). GPS ZTD has high temporal resolution (5 min), thus the main limitation is the station density. GPS can be combined with other independent correction datasets or used to validate other independent correction datasets at point locations.

5. Conclusions

Tropospheric noise greatly limits the range of signals that can be measured using InSAR, and impacts the degree of confidence that we can place on inferred properties of Earth's behavior. There is currently little consensus among InSAR users on the optimal ways to mitigate tropospheric effects, or on how to evaluate the performance of those approaches. Working towards such a consensus, we have summarized and tested some of the most common methods used to remove tropospheric noise as well as the methods used to assess the quality of the removal. We applied our approach to interferograms from two field areas that sample very distinct topographic and atmospheric regimes and come to the following conclusions:

- The acquisition time of a given SAR image relative to the time period constrained by a given correction dataset impacts the quality of the correction. The time difference between weather reanalysis models and our SAR acquisitions was within 28 and 48 min. If the SAR acquisition time for a particular area were farther in time from the model output, a worse result would generally be expected – particularly at short spatial scales. We recommend prioritizing correction methods that are valid at times closest to the SAR acquisition time.
- Weather models that are customized for the particular region could be expected to improve the results even further. In our case, daytime/cloud-free MODIS imagery was not available within few hours of the SAR acquisition for many dates. Previous studies with MERIS/ASAR data for the ENVISAT platform demonstrated that, after correction using observations taken at the same time as the SAR imagery, the corrected observations approached the theoretical accuracy of the MERIS retrieval (Li et al., 2006).
- We found that the GACOS correction – which uses the ECMWF-operational model and elevation data – performs best out of all tested methods in both study areas. We also found that GPS-derived corrections performed comparably well when and where data was available. At the time of this publication there are plans to integrate GNSS into the GACOS products, but the examples shown in this paper do not include any contribution from GNSS observations.
- A combination of the GACOS model with GNSS ZTD observations is likely an optimal solution given the data and methods we tested. Furthermore, this approach will continue to become more feasible as global GNSS networks continue to expand.
- None of the corrections explored here are effective at removing the impact of lateral variations in tropospheric properties over spatial scales smaller than ~75 km. The impact of tropospheric noise at smaller spatial scales that is due to topography can be reduced in certain cases.
- Elevation-phase dependence is a more useful metric for areas of high relief (such as south-central Mexico) and less effective in areas of low relief (such as the central US). When studying large areas it is beneficial to account for the spatial variability of the elevation-phase correlation.
- Distance-dependent functions are useful for rapid assessment of the

quality of a given correction and should be used routinely when applying corrections. The empirical semivariogram tends to best capture spatial variations because it explicitly samples only pixels separated by a given distance range, whereas the windowed standard deviation outputs the average of all spatial scales smaller than the given window size. The semivariogram approach makes it easy to recognize the remaining tropospheric signal that was not removed by a given correction – primarily the short spatial scale signals due to turbulent troposphere and/or areas of precipitation.

- The semi-variogram approach is more flexible and easier to apply than spectral analysis in regions with irregularly-spaced data. The improvement that is evident through inspection of the semi-variograms is not as clear when looking at the spectral analysis results (Figs. 7 and 8).

No one method will consistently remove all contributions from the troposphere from any given interferogram. Quantitative assessment of correction performance allows the researcher to interpret only the robust features in their interferograms or time series, and may be particularly important in the identification of seasonal signals, or signals that correlate with topography. With the Sentinel-1a/b constellation and upcoming missions such as the NASA/ISRO Synthetic Aperture Radar, data volumes are continuously increasing. The provision of tropospheric and/or ionospheric corrections as a layer will enable researchers to focus on the interpretation of ground displacement or land surface change - however, it will be critical to have a clear understanding of the performance of such corrections. Future efforts that focus on combinations of these tropospheric mitigation approaches, and on their evaluation, will be key to the full utilization of the rich set of SAR data that is now becoming freely and openly available.

Acknowledgements

Part of the research was carried out at the Jet Propulsion Laboratory, California Institute of Technology, under a contract with the National Aeronautics and Space Administration.

This work was partially supported by the JPL Strategic University Research Partnerships (SURP) program and NASA grants NNX16AL20G and NNX16AK57G. GACOS products were provided by Newcastle University at http://ceg-research.ncl.ac.uk/v2/gacos. MODIS data were provided by NASA EarthData at https://ladsweb.modaps.eosdis.nasa.gov. NARR products were provided by the NOAA-ESRL Physical Sciences Division, Boulder, CO at http://www.esrl.noaa.gov/psd/thredds/dodsC/Datasets/NARR. MERRA-2 products were available at MDISC at https://goldsmr3.gesdisc.eosdis.nasa.gov, managed by the NASA Goddard Earth Sciences (GES) Data and Information Services Center (DISC). ERA-I data was provided by European Centre for Medium-Range Weather Forecasts (ECMWF) at https://apps.ecmwf.int/datasets/data. Copernicus Sentinel-1 SAR imagery used in this study is from the European Space Agency (ESA), downloaded through the Alaska Satellite Facility (ASF) at https://vertex.daac.asf.alaska.edu. We also thank the Jet Propulsion Laboratory for providing us with ISCE (Rosen et al., 2012), the stack processing capability (Fattahi et al., 2017), and the SRTM topographic data (Farr et al., 2007). We acknowledge the Nevada Geodetic Laboratory at the University of Nevada, Reno for providing us with zenith tropospheric GPS estimates ftp://gneiss.nbmg.unr.edu/trop. We thank the many institutions that support the GPS networks used in the paper, including the Oklahoma and Texas Departments of Transportation, University of Oklahoma, University of Colorado, University Corporation for Atmospheric Research (UCAR), Topcon TopNET live, SmartNet North America, and the National Geodetic (NGS)/NOAA for supporting the Continuously Operating Reference Station (CORS). All figures were prepared using the 2D graphics module for Python, Matplotlib (Hunter, 2007), and the free and open source vector graphics editor, Inkscape. Finally, we thank the reviewers and editors for their very helpful comments and suggestions.

Appendix A. Supplementary data

Supplementary data to this article can be found online at https://doi.org/10.1016/j.rse.2019.111326.

References

Agram, P.S., Jolivet, R., Riel, B., Lin, Y.N., Simons, M., Hetland, E., Doin, M.-P., Lasserre, C., 2013. New radar interferometric time series analysis toolbox released. EOS Trans. Am. Geophys. Union 94, 69–70. https://doi.org/10.1002/2013EO070001.

Amelung, F., Galloway, D.L., Bell, J.W., Zebker, H.A., Laczniak, R.J., 1999. Sensing the ups and downs of Las Vegas: InSAR reveals structural control of land subsidence and aquifer-system deformation. Geology 27, 483–486. https://doi.org/10.1130/0091-7613(1999)027<0483:STUADO>2.3.CO;2.

Barnhart, W.D., Yeck, W.L., McNamara, D.E., 2018. Induced earthquake and liquefaction hazards in Oklahoma, USA: constraints from InSAR. Remote Sens. Environ. 218, 1–12. https://doi.org/10.1016/j.rse.2018.09.005.

Beauducel, F., Briole, P., Froger, J.-L., 2000. Volcano-wide fringes in ERS synthetic aperture radar interferograms of Etna (1992–1998): deformation or tropospheric effect? J. Geophys. Res. Solid Earth 105, 16391–16402. https://doi.org/10.1029/2000JB900095.

Bekaert, D.P.S., Hooper, A., Wright, T.J., 2015a. A spatially variable power law tropospheric correction technique for InSAR data. J. Geophys. Res. Solid Earth 120, 1345–1356.

Bekaert, D.P.S., Hooper, A., Wright, T.J., 2015b. Reassessing the 2006 Guerrero slow-slip event, Mexico: implications for large earthquakes in the Guerrero Gap. J. Geophys. Res. Solid Earth 120, 1357–1375.

Bekaert, D.P.S., Walters, R.J., Wright, T.J., Hooper, A.J., Parker, D.J., 2015c. Statistical comparison of InSAR tropospheric correction techniques. Remote Sens. Environ. 170, 40–47. https://doi.org/10.1016/j.rse.2015.08.035.

Bekaert, D.P.S., Hamlington, B.D., Buzzanga, B., Jones, C.E., 2017. Spaceborne synthetic aperture radar survey of subsidence in Hampton Roads, Virginia (USA). Sci. Rep. 7, 14752. https://doi.org/10.1038/s41598-017-15309-5.

Berrada Baby, H., Golé, P., Lavergnat, J., 1988. A model for the tropospheric excess path length of radio waves from surface meteorological measurements. Radio Sci. 23, 1023–1038. https://doi.org/10.1029/RS023i006p01023.

Bevis, M., Businger, S., Herring, T.A., Rocken, C., Anthes, R.A., Ware, R.H., 1992. GPS meteorology: remote sensing of atmospheric water vapor using the Global Positioning System. J. Geophys. Res. Atmospheres 97, 15787–15801.

Blewitt, G., Hammond, W.C., Kreemer, C., 2018. Harnessing the GPS data explosion for interdisciplinary science. Eos 99.

Carlson, T.N., 1991. Mid-latitude Weather Systems.

Cavalie, O., Doin, M.-P., Lasserre, C., Briole, P., 2007. Ground motion measurement in the Lake Mead area, Nevada, by differential synthetic aperture radar interferometry time series analysis: probing the lithosphere rheological structure. J. Geophys. Res.-Solid Earth 112. https://doi.org/10.1029/2006JB004344.

Chaussard, E., Amelung, F., Aoki, Y., 2013. Characterization of open and closed volcanic systems in Indonesia and Mexico using InSAR time series: InSAR time series in Indonesia and Mexico. J. Geophys. Res. Solid Earth 118, 3957–3969. https://doi.org/10.1002/jgrb.50288.

Chaussard, E., Milillo, P., Bürgmann, R., Perissin, D., Fielding, E.J., Baker, B., 2017. Remote sensing of ground deformation for monitoring groundwater management practices: application to the Santa Clara Valley during the 2012–2015 California drought. J. Geophys. Res. Solid Earth 122, 8566–8582.

De Zan, F., Guarnieri, A.M., 2006. TOPSAR: terrain observation by progressive scans. IEEE Trans. Geosci. Remote Sens. 44, 2352–2360.

Dee, D.P., Uppala, S.M., Simmons, A.J., Berrisford, P., Poli, P., Kobayashi, S., Andrae, U., Balmaseda, M.A., Balsamo, G., Bauer, D.P., 2011. The ERA-Interim reanalysis: configuration and performance of the data assimilation system. Q. J. R. Meteorol. Soc. 137, 553–597.

Doin, M.-P., Lasserre, C., Peltzer, G., Cavalié, O., Doubre, C., 2009. Corrections of stratified tropospheric delays in SAR interferometry: validation with global atmospheric models. J. Appl. Geophys. 69, 35–50. https://doi.org/10.1016/j.jappgeo.2009.03.010.

Elliott, J.R., Biggs, J., Parsons, B., Wright, T.J., 2008. InSAR slip rate determination on the Altyn Tagh Fault, northern Tibet, in the presence of topographically correlated atmospheric delays. Geophys. Res. Lett. 35.

Ellsworth, W.L., 2013. Injection-induced earthquakes. Science 341, 1225942. https://doi.org/10.1126/science.1225942.

Emardson, T.R., Simons, M., Webb, F.H., 2003. Neutral atmospheric delay in interferometric synthetic aperture radar applications: statistical description and mitigation. J. Geophys. Res. 108, 2231. https://doi.org/10.1029/2002JB001781.

European Space Agency, 2013. Sentinel-1 User Handbook.

Farr, T.G., Rosen, P.A., Caro, E., Crippen, R., Duren, R., Hensley, S., Kobrick, M., Paller, M., Rodriguez, E., Roth, L., Seal, D., Shaffer, S., Shimada, J., Umland, J., Werner, M., Oskin, M., Burbank, D., Alsdorf, D., 2007. The Shuttle Radar Topography Mission. Rev. Geophys. 45. https://doi.org/10.1029/2005RG000183.

Fattahi, H., Amelung, F., 2014. InSAR uncertainty due to orbital errors. Geophys. J. Int. 199, 549–560. https://doi.org/10.1093/gji/ggu276.

Fattahi, H., Agram, P., Simons, M., 2017. A network-based enhanced spectral diversity approach for TOPS time-series analysis. IEEE Trans. Geosci. Remote Sens. 55, 777–786.

Ferretti, A., Prati, C., Rocca, F., 2001. Permanent scatterers in SAR interferometry. IEEE Trans. Geosci. Remote Sens. 39, 8–20. https://doi.org/10.1109/36.898661.

Ferretti, A., Fumagalli, A., Novali, F., Prati, C., Rocca, F., Rucci, A., 2011. A new algorithm for processing interferometric data-stacks: SqueeSAR. IEEE Trans. Geosci. Remote Sens. 49, 3460–3470. https://doi.org/10.1109/TGRS.2011.2124465.

Fialko, Y., 2006. Interseismic strain accumulation and the earthquake potential of the

southern San Andreas fault system. Nature 441, 968–970.
Fielding, E.J., Sangha, S.S., Bekaert, D.P., Samsonov, S.V., Chang, J.C., 2017. Surface deformation of north-central Oklahoma related to the 2016 M w 5.8 Pawnee earthquake from SAR interferometry time series. Seismol. Res. Lett. 88, 971–982.
Foster, J., Brooks, B., Cherubini, T., Shacat, C., Businger, S., Werner, C.L., 2006. Mitigating atmospheric noise for InSAR using a high resolution weather model. Geophys. Res. Lett. 33.
Fournier, T., Pritchard, M.E., Finnegan, N., 2011. Accounting for atmospheric delays in InSAR data in a search for long-wavelength deformation in South America. IEEE Trans. Geosci. Remote Sens. 49, 3856–3867. https://doi.org/10.1109/TGRS.2011.2139217.
Funning, G.J., Parsons, B., Wright, T.J., Jackson, J.A., Fielding, E.J., 2005. Surface displacements and source parameters of the 2003 Bam (Iran) earthquake from Envisat advanced synthetic aperture radar imagery. J. Geophys. Res. 110, B09406. https://doi.org/10.1029/2004JB003338.
Goldstein, R., 1995. Atmospheric limitations to repeat-track radar interferometry. Geophys. Res. Lett. 22, 2517–2520.
Grandin, R., Vallée, M., Lacassin, R., 2017. Rupture process of the Mw 5.8 Pawnee, Oklahoma, earthquake from Sentinel-1 InSAR and seismological data. Seismol. Res. Lett. 88, 994–1004.
Hanssen, R.F., 2001. Radar Interferometry: Data Interpretation and Error Analysis. Springer.
Hanssen, R., Bamler, R., 1999. Evaluation of interpolation kernels for SAR interferometry. IEEE Trans. Geosci. Remote Sens. 37, 318–321.
Hetland, E.A., Musé, P., Simons, M., Lin, Y.N., Agram, P.S., DiCaprio, C.J., 2012. Multiscale InSAR Time Series (MInTS) analysis of surface deformation. J. Geophys. Res. Solid Earth 117https://doi.org/10.1029/2011JB008731. n/a–n/a.
Holland, A.A., 2013. Earthquakes triggered by hydraulic fracturing in south-central Oklahoma. Bull. Seismol. Soc. Am. 103, 1784–1792.
Hooper, A., Zebker, H., Segall, P., Kampes, B., 2004. A new method for measuring deformation on volcanoes and other natural terrains using InSAR persistent scatterers. Geophys. Res. Lett. 31, L23611. https://doi.org/10.1029/2004GL021737.
Hooper, A., Bekaert, D., Spaans, K., Arikan, M., 2012. Recent advances in SAR interferometry time series analysis for measuring crustal deformation. Tectonophysics 514–517 (1–13).
Horton, S., 2012. Disposal of hydrofracking waste fluid by injection into subsurface aquifers triggers earthquake swarm in central Arkansas with potential for damaging earthquake. Seismol. Res. Lett. 83, 250–260.
Houlié, N., Funning, G.J., Bürgmann, R., 2016. Use of a GPS-derived troposphere model to improve InSAR deformation estimates in the San Gabriel Valley, California. IEEE Trans. Geosci. Remote Sens. 54, 5365–5374. https://doi.org/10.1109/TGRS.2016.2561971.
Hunter, J.D., 2007. Matplotlib: a 2D graphics environment. Comput. Sci. Eng. 9, 90–95. https://doi.org/10.1109/MCSE.2007.55.
Hussain, E., Wright, T.J., Walters, R.J., Bekaert, D.P.S., Lloyd, R., Hooper, A., 2018. Constant strain accumulation rate between major earthquakes on the North Anatolian Fault. Nat. Commun. 9, 1392. https://doi.org/10.1038/s41467-018-03739-2.
Jolivet, R., Grandin, R., Lasserre, C., Doin, M.-P., Peltzer, G., 2011. Systematic InSAR tropospheric phase delay corrections from global meteorological reanalysis data. Geophys. Res. Lett. 38. https://doi.org/10.1029/2011GL048757.
Jones, C.E., An, K., Blom, R.G., Kent, J.D., Ivins, E.R., Bekaert, D., 2016. Anthropogenic and geologic influences on subsidence in the vicinity of New Orleans, Louisiana. J. Geophys. Res. Solid Earth 121, 3867–3887.
Keranen, K.M., Weingarten, M., 2018. Induced seismicity. Annu. Rev. Earth Planet. Sci. 46, 149–174.
Lanari, R., Casu, F., Manzo, M., Zeni, G., Berardino, P., Manunta, M., Pepe, A., 2007. An overview of the small baseline subset algorithm: a DInSAR technique for surface deformation analysis. Pure Appl. Geophys. 164, 637–661. https://doi.org/10.1007/s00024-007-0192-9.
Li, Z., Muller, J.-P., Cross, P., 2003. Comparison of precipitable water vapor derived from radiosonde, GPS, and Moderate-Resolution Imaging Spectroradiometer measurements. J. Geophys. Res. Atmospheres 108, 4651. https://doi.org/10.1029/2003JD003372.
Li, Z., Muller, J.-P., Cross, P., Fielding, E.J., 2005. Interferometric synthetic aperture radar (InSAR) atmospheric correction: GPS, Moderate Resolution Imaging Spectroradiometer (MODIS), and InSAR integration. J. Geophys. Res. Solid Earth 110, B03410. https://doi.org/10.1029/2004JB003446.
Li, Z., Muller, J.P., Cross, P., Albert, P., Fischer, J., Bennartz, R., 2006. Assessment of the potential of MERIS near-infrared water vapour products to correct ASAR interferometric measurements. Int. J. Remote Sens. 27, 349–365. https://doi.org/10.1080/01431160500307342.
Li, Z.W., Ding, X.L., Huang, C., Zou, Z.R., Chen, Y.L., 2007. Atmospheric effects on repeat-pass InSAR measurements over Shanghai region. J. Atmospheric Sol.-Terr. Phys. 69, 1344–1356.
Liang, H., et al., 2018. Toward mitigating stratified tropospheric delays in multitemporal InSAR: a quadtree aided joint model. IEEE Trans. Geosci. Remote Sens. 99, 1–13.
Lin, Y.N., Simons, M., Hetland, E.A., Muse, P., DiCaprio, C., 2010. A multiscale approach to estimating topographically correlated propagation delays in radar interferograms. Geochem. Geophys. Geosystems 11.
Lindsey, E.O., Fialko, Y., Bock, Y., Sandwell, D.T., Bilham, R., 2014. Localized and distributed creep along the southern San Andreas Fault. J. Geophys. Res. Solid Earth 119, 7909–7922. https://doi.org/10.1002/2014JB011275.
Lindsey, E.O., Natsuaki, R., Xu, X., Shimada, M., Hashimoto, M., Melgar, D., Sandwell, D.T., 2015. Line-of-sight displacement from ALOS-2 interferometry: M_w 7.8 Gorkha Earthquake and M_w 7.3 aftershock. Geophys. Res. Lett. 42, 6655–6661. https://doi.org/10.1002/2015GL065385.
Lohman, R.B., Simons, M., 2005. Some thoughts on the use of InSAR data to constrain models of surface deformation: noise structure and data downsampling. Geochem. Geophys. Geosyst. 6, 12.
Lohman, R.B., Simons, M., Savage, B., 2002. Location and mechanism of the Little Skull Mountain earthquake as constrained by satellite radar interferometry and seismic waveform modeling. J. Geophys. Res. 107 (7–1).
Lu, Z., Dzurisin, D., 2010. Ground surface deformation patterns, magma supply, and magma storage at Okmok volcano, Alaska, from InSAR analysis: 2. Coeruptive deflation, July–August 2008. J. Geophys. Res. 115. https://doi.org/10.1029/2009JB006970.
Lundgren, P., Casu, F., Manzo, M., Pepe, A., Berardino, P., Sansosti, E., Lanari, R., 2004. Gravity and magma induced spreading of Mount Etna volcano revealed by satellite radar interferometry. Geophys. Res. Lett. 31, L04602. https://doi.org/10.1029/2003GL018736.
Massonnet, D., Rossi, M., Carmona, C., Adragna, F., Peltzer, G., Feigl, K., Rabaute, T., 1993. The displacement field of the Landers earthquake mapped by radar interferometry. Nature 364, 138–142. https://doi.org/10.1038/364138a0.
Murray, K.D., Lohman, R.B., 2018. Short-lived pause in Central California subsidence after heavy winter precipitation of 2017. Sci. Adv. 4, eaar8144. https://doi.org/10.1126/sciadv.aar8144.
Onn, F., Zebker, H.A., 2006. Correction for interferometric synthetic aperture radar atmospheric phase artifacts using time series of zenith wet delay observations from a GPS network. J. Geophys. Res. Solid Earth 111. https://doi.org/10.1029/2005JB004012.
Osmanoğlu, B., Dixon, T.H., Wdowinski, S., Cabral-Cano, E., Jiang, Y., 2011. Mexico City subsidence observed with persistent scatterer InSAR. Int. J. Appl. Earth Obs. Geoinformation 13, 1–12.
Pritchard, M.E., Simons, M., 2002. A satellite geodetic survey of large-scale deformation of volcanic centres in the central Andes. Nature 418, 167.
Pritchard, M.E., Simons, M., Rosen, P.A., Hensley, S., Webb, F.H., 2002. Co-seismic slip from the 1995 July 30 Mw = 8.1 Antofagasta, Chile, earthquake as constrained by InSAR and GPS observations. Geophys. J. Int. 150, 362–376. https://doi.org/10.1046/j.1365-246X.2002.01661.x.
Puysségur, B., Michel, R., Avouac, J.-P., 2007. Tropospheric phase delay in interferometric synthetic aperture radar estimated from meteorological model and multispectral imagery. J. Geophys. Res. Solid Earth 112. https://doi.org/10.1029/2006JB004352.
Remy, D., Bonvalot, S., Briole, P., Murakami, M., 2003. Accurate measurements of tropospheric effects in volcanic areas from SAR interferometry data: application to Sakurajima volcano (Japan). Earth Planet. Sci. Lett. 213, 299–310. https://doi.org/10.1016/S0012-821X(03)00331-5.
Reuveni, Y., Bock, Y., Tong, X., Moore, A.W., 2015. Calibrating interferometric synthetic aperture radar (InSAR) images with regional GPS network atmosphere models. Geophys. J. Int. 202, 2106–2119. https://doi.org/10.1093/gji/ggv253.
Rosen, P.A., Gurrola, E., Sacco, G.F., Zebker, H., 2012. The InSAR scientific computing environment. In: EUSAR 2012; 9th European Conference on Synthetic Aperture Radar. Presented at the EUSAR 2012; 9th European Conference on Synthetic Aperture Radar, pp. 730–733.
Scott, C.P., Lohman, R.B., 2016. Sensitivity of earthquake source inversions to atmospheric noise and corrections of InSAR data. J. Geophys. Res. Solid Earth 121, 2016JB012969. https://doi.org/10.1002/2016JB012969.
Shen, L., Hooper, A., Elliott, J., 2019. A spatially varying scaling method for InSAR tropospheric corrections using a high-resolution weather model. Journal of Geophysical Research: Solid Earth 124 (4), 4051–4068.
Smith, E.K., Weintraub, S., 1953. The constants in the equation for atmospheric refractive index at radio frequencies. Proc. IRE 41, 1035–1037.
Talebian, M., Fielding, E.J., Funning, G.J., Ghorashi, M., Jackson, J., Nazari, H., Parsons, B., Priestley, K., Rosen, P.A., Walker, R., Wright, T.J., 2004. The 2003 Bam (Iran) earthquake: rupture of a blind strike-slip fault. Geophys. Res. Lett. 31.
Tymofyeyeva, Ekaterina, Fialko, Yuri, 2015. Mitigation of atmospheric phase delays in InSAR data, with application to the eastern California shear zone. Journal of Geophysical Research: Solid Earth 120 (8), 5952–5963.
Wicks, C., Thatcher, W., Dzurisin, D., 1998. Migration of fluids beneath Yellowstone caldera inferred from satellite radar interferometry. Science 282, 458–462. https://doi.org/10.1126/science.282.5388.458.
Wicks, C.W., Dzurisin, D., Ingebritsen, S., Thatcher, W., Lu, Z., Iverson, J., 2002. Magmatic activity beneath the quiescent Three Sisters volcanic center, central Oregon Cascade Range, USA. Geophys. Res. Lett. 29, 26-1-26–4. https://doi.org/10.1029/2001GL014205.
Williams, S., Bock, Y., Fang, P., 1998. Integrated satellite interferometry: tropospheric noise, GPS estimates and implications for interferometric synthetic aperture radar products. J. Geophys. Res.-Solid Earth 103, 27051–27067. https://doi.org/10.1029/98JB02794.
Yeck, W.L., Hayes, G.P., McNamara, D.E., Rubinstein, J.L., Barnhart, W.D., Earle, P.S., Benz, H.M., 2017. Oklahoma experiences largest earthquake during ongoing regional wastewater injection hazard mitigation efforts. Geophys. Res. Lett. 44, 711–717. https://doi.org/10.1002/2016GL071685.
Yu, C., Li, Z., Penna, N.T., Crippa, P., 2018. Generic atmospheric correction model for interferometric synthetic aperture radar observations. J. Geophys. Res. Solid Earth 123, 9202–9222. https://doi.org/10.1029/2017JB015305.
Zebker, H.A., Rosen, P.A., Hensley, S., 1997. Atmospheric effects in interferometric synthetic aperture radar surface deformation and topographic maps. J. Geophys. Res. 102, 7547–7563.